Structural and optical properties of a mechanically alloyed thermoelectric lamellar SnSeS solid solution

M. O. Melquíades, L. S. de Oliveira (iD), Q. H. F. Rebelo, P. Chaudhuri, E. R. Leite, D. M. Trichês, and S. Michielon de Souza (iD)

View Online   **Export Citation**   **CrossMark**

ARTICLES YOU MAY BE INTERESTED IN

Lock-in Amplifiers

Zurich Instruments

Watch the Video ▶

Structural and optical properties of a mechanically alloyed thermoelectric lamellar SnSeS solid solution

View Online   Export Citation   CrossMark

M. O. Melquíades,[1] L. S. de Oliveira,[1,2] [ID] Q. H. F. Rebelo,[3,4] P. Chaudhuri,[1] E. R. Leite,[5,6] D. M. Trichês,[1,3] and S. Michielon de Souza[1,3,a)] [ID]

AFFILIATIONS

[1]Postgraduation Program in Material Science & Engineering, Federal University of Amazonas (UFAM), Manaus, Amazonas 69077-000, Brazil
[2]Center for Natural and Human Sciences (CCNH), Federal University of ABC (UFABC), Santo André, São Paulo 09210-580, Brazil
[3]Federal University of Amazonas (UFAM), Manaus, Amazonas 69077-000, Brazil
[4]Federal University of Western Pará (UFOPA), Santarém, Pará 68035-110, Brazil
[5]Federal University of São Carlos (UFSCar), São Carlos, São Paulo 13565-905, Brazil
[6]Brazilian Nanotechnology National Laboratory (LNNano)/CNPEM, Campinas, São Paulo 13083-970, Brazil

[a)]Author to whom correspondence should be addressed: michielon@ufam.edu.br

ABSTRACT

A chalcogenide $SnS_{2-x}Se_x$ alloy with x = 1, synthesized by high-energy mechanical alloying, was characterized by high-resolution transmission electron microscopy, X-ray diffraction, differential scanning calorimetry, Raman spectroscopy, and UV-Vis absorbance. The obtained alloy powder was a lamellar solid solution with nanometric crystalline domain sizes and several types of defects such as stacked faults, discordances, crystal fractures, and local atomic disorders. All of these microstructural features lead to the manifestation of different optical and vibrational properties of this extensively deformed nanostructured sample. Raman spectroscopic measurements suggested a two-mode vibration indicating how the S and Se atoms were distributed in the crystalline lattice. The UV-Vis absorbance spectrum showed multiple bandgaps at 1.99, 2.60, 3.09, 3.66, and 4.56 eV that may well be described as direct allowed interband electronic transitions suggesting inhomogeneous strain and domains.

I. INTRODUCTION

Layered chalcogenide and dichalcogenide materials like SnSe, SnS, $SnSe_2$, and SnS_2 show several types of structural complexity formed mainly by two-dimensional atomic arrangements. They are composed of earth-abundant and eco-friendly materials. These materials are characterized by many interesting thermoelectric[1,2] and optical properties,[3,4] depending on their structural shape, size, and chemical compositions. A good thermoelectric material must necessarily possess a large electrical conductivity and low thermal conductivity. These properties are related, and it is difficult to control them independently. However, the thermal conductivity has a vibrational component (phonons), and is, therefore, independent of the electrical conductivity. In this case, a suitable strategy to improve the thermoelectricity of the material is to introduce structural defects that may act as phonon scattering centers impairing the vibrational thermal conductivity.

In general, the solid solutions possess low thermal conductivity compared to that of the constituent compounds because of the phonon scattering from disordered atoms.[5] Very recently, it has been reported that thermal conductivity decreases with increasing amounts of Se(x) in an orthorhombic $SnS_{1-x}Se_x$ $(0 \leq x \leq 1)$ solid solution produced by mechanical alloying (MA) and spark plasma sintering.[6] It has been reported earlier that in hexagonal $SnS_{2-x}Se_x$ $(0 \leq x \leq 2)$ solid solutions, the bandgaps can be discretely modulated with the increase of Se content.[7] In fact, the modified materials based on 2D crystals would provide diversified strategies for electronic structure engineering and efficient applications in electronic and optoelectronic devices.

SnX_2 (X = S, Se) can be grown in various polytype structures.[8] The simplest possible polytype, $2H$-SnX_2, crystalizes in a lattice that belongs to the space group $P\bar{3}m1$ (No. 164), in the Strukturbericht designation C6, CdI_2 prototype. These materials form X–Sn–X-type layered structures, with the chalcogenide atoms in two hexagonal planes separated by a plane of metal atoms. Adjacent layers are bound by weak van der Waals interactions.[9]

The properties of the layered materials depend strongly on the methods of preparation. The technique of mechanical alloying (MA) is effective in obtaining nanostructured,[10] supersaturated,[11] and substituted solid solutions. MA is concerned with the chemical transformations induced by mechanical means, such as compression, shear, or friction.

In this work, we have produced the highest possible level of the chemical disorder by fixing the stoichiometry of the $SnS_{2-x}Se_x$ solid solution with x = 1. Thus, the Wyckoff sites 2a and 2d are equally occupied by Se and S atoms. The sample underwent 100 h of high-energy mechanical alloying, in order to reach a high concentration of structural defects besides guaranteeing homogeneity. The obtained samples were investigated by X-ray diffraction (XRD), high-resolution transmission electron microscopy (HRTEM), Raman spectroscopy, UV-Vis, and differential scanning calorimetry (DSC) measurements.

II. EXPERIMENTAL PROCEDURE

The samples were produced from binary mixtures of Sn (Alfa Aesar, 99.999%), Se (Alfa Aesar, 99.999%), and S (Alfa Aesar, 99.999%) powders, with nominal compositions $Sn_{34}Se_{33}S_{33}$ (SnSeS). The precursor powders were sealed together with several steel balls in a cylindrical steel vial followed by mechanical alloying. The ball-to-powder weight ratio (BPR) was 7:1. A Spex Mixer/Mill model 8000 was used to obtain the MA sample at room temperature. Three different samples were produced. Two of them were produced without atmospheric control by milling of 1 (S-1 h) and 10 h (S-10 h), respectively. The third sample was prepared by 100 h (S-100 h) of milling in the presence of argon gas in order to avoid the process of oxidation.

X-ray powder diffraction data were collected on Empyrean diffractometer, from Panalytical, operating in the reflection mode, using CuK$_{\alpha 1}$ radiation ($\lambda = 1.54056$ Å), an accelerating voltage of 40 kV and current of 40 mA, equipped with a Bragg-Brentano HD mirror, a 0.02 rad soller slit, a 1° antiscattering slit and 1/4° divergence slit in the incident beam. A 0.04 rad soller slit and a 9 mm antiscattering slit were used in the diffracted. The X-ray photons were detected with an area detector type (PIXcel3D-Medipix3 1×1 detector). Measurements were performed in the angular range from 10° to 100° (2θ), with step sizes of 0.01313° with 60 s each step. The Rietveld method[12] implemented in the GSAS software package[13] was used to refine the structural parameters and line widths from the XRD patterns, following the recommendations of the IUCr.[14] Six-term Chebyschev polynomials were used to fit the Compton scattering plus background radiations. The peak profile analysis was carried out using the modified Thompson–Cox–Hasting pseudo-Voigt profile function (CW profile function 4 in the GSAS package), which considers the anisotropic microstrain by Stephens's model[15,16] and texture effects.

In the CW profile function 4, the Gaussian (Γ_G) and Lorentzian (Γ_L) contributions from FWHM are expressed as follows:

$$\Gamma_G = \left[(U + (1-\eta)^2 d_{hkl}^4 \Gamma_S^2(h\,k\,l))\tan^2\theta + V\tan\theta + W + \frac{P}{\cos^2\theta} \right]^{1/2}, \tag{1}$$

$$\Gamma_L = \eta d_{hkl}^2 \Gamma_S(h\,k\,l)\tan\theta + \frac{X + X_e\cos\phi}{\cos\theta}, \tag{2}$$

where the parameter η is a "mixing coefficient" that determines the contributions of the Gaussian ($\eta = 0$) and Lorentzian ($\eta = 1$) broadening; d_{hkl} is the distance between the lattice planes and θ is the Bragg angle. In the Gaussian part, the parameters V and W depend on the instruments. The parameters P and the term $X + X_e\cos\phi$ describe the Gaussian and the Lorentzian contributions to size broadening, respectively. The parameters P and X correspond to isotropic crystallite-size broadening, while X_e expresses anisotropic crystallite-size effects; ϕ is the angle between a reflection vector and its respective broadening axis. The isotropic and anisotropic U and $\Gamma_S(h\,k\,l)$ strain parameters express peak broadening caused by strains in the crystal lattice. $\Gamma_S(h\,k\,l)$ is an $h\,k\,l$-dependent line broadening function that depends on the crystal symmetry.[16] In our study, the instrumental broadening was analyzed by a certified LaB$_6$ standard (NIST 660b) and the obtained values of $U = 0.0$, $V = -0.0036$, $W = 0.0023$ remained unaltered. The disagreement of the relative intensities of the relevant $h\,k\,l$ reflections was considered by using spherical harmonics preferential orientation model (ODF).[17]

In the pseudo-Voigt function, the Lorentzian (β_L) and Gaussian (β_G) integral breadths of the diffraction simulated line can be calculated by using the full width at half maximum (Γ) and mixture coefficient η parameter, obtained directly from the Rietveld analysis as[13]

$$\beta_G = \frac{\Gamma}{2} \sqrt{\frac{\pi(1 - 0.74417\eta - 0.24781\eta^2 - 0.00810\eta^3)}{\ln 2}} \tag{3}$$

and

$$\beta_L = \frac{\pi\Gamma}{2}(0.72928\eta + 0.19289\eta^2 + 0.07783\eta^3). \tag{4}$$

So, the mean crystallite size $\langle D \rangle$ and microstrain $\langle \varepsilon \rangle$ were calculated by using Scherrer's equation with Γ obtained from the best adjusted peaks,

$$D_{(hkl)} = \frac{0.91\lambda}{\beta_L\cos\theta} \tag{5}$$

and

$$\varepsilon_{(hkl)} = \beta_G/4\tan\theta. \tag{6}$$

All atomic displacements were considered isotropic and fixed at 0.025 Å.[2]

The thermal behavior of the samples was investigated by DSC thermograms in a Netzsch 3500 Sirius model, under flowing argon

in aluminum pans, from 50 °C until 520 °C using a 10 °C/min heating rate.

The Raman spectrum was recorded on a Labram iHR550 triple spectrometer (Horiba Jobin-Yvon, Japan) equipped with a 5.0 mW He-Ne laser ($\lambda = 632.81$ nm) and a liquid-nitrogen-cooled CCD. The Raman frequencies were determined from a fit of the peaks to a Lorentzian profile.

The high-resolution transmission electron microscopy images were taken at the Interdisciplinary Laboratory of Electrochemistry and Ceramics—LIEC/ UFSCar using a TECNAI F20 FEI microscope which was operated with 200 kV. The analysis of the figures was performed by using the open source Java-based image processing *program* ImageJ.[18]

The crystalline powders were diluted in water followed by simple/ordinary filtration using a $0.22 \, \mu m$ diameter filter paper. A small quantity was put in a quartz cuvette in order to measure the absorbance $Abs(\lambda)$ in the wavelength range between 200 and $1100 \, nm^{-1}$. Absorbance measurements were performed on a UV-Vis spectrophotometer (Global Trade Technology, Brazil).

The bandgap energy values can be obtained by a Tauc[19] analysis of the absorption edge through the equation

$$\alpha h\nu = C(h\nu - E_g)^{1/n}, \tag{7}$$

where α is the absorption coefficient, h is the Planck constant, ν is the frequency, and C is a constant.[20] The values of n for allowed direct, allowed indirect, forbidden direct, and forbidden indirect transition are 2, 1/2, 2/3, and 1/3, respectively. The relationship between absorption coefficient, thickness of the sample (d), and the experimental absorbance $Abs(\lambda)$ is given by $\alpha = (2.303/d)Abs(\lambda)$.[21] So, the dependence of the absorbance $Abs(\lambda)$ on the photon energy, can be expressed as

$$Abs(\lambda)h\nu = B(h\nu - E_g)^{1/n}, \tag{8}$$

where $B = Cd/2.303$ is a new constant associated with the thickness of the sample and should be included in the fitting procedure.[22]

For the bandgap energy (E_g) of the S-100 h sample, the dependence of the absorbance $Abs(\lambda)$ on the photon energy was calculated by fitting the straights regions of the $(Abs(\lambda)h\nu)^n$ vs $h\nu$ graph and extrapolating the straight-line portion to the $h\nu$ axis. In our sample, the best agreement was obtained for $n = 2$.[20]

III. RESULTS AND DISCUSSION

Figure 1 shows the production of the S-100 h sample. In Fig. 1(a), we show the XRD patterns of S-1 h (room atmosphere) and S-100 h (argon atmosphere) samples. As we can see, both S-1 h and S-100 h XRD patterns have enlarged and asymmetric peaks, alternating between sharp and broad profiles. This indicates an anisotropic nanometric structure, since $h \, k \, l$-dependent peak broadening and asymmetries are commonly associated with stacking fault defects.

The presence of stacking fault in small crystals makes the analysis of XRD patterns difficult. However, it is clear that the intense peak in low angle corresponds to the plane (0 0 1), parallel to the SnSeS layer crystals (ICSD Card No. 650864).[23] In fact, the

similarities between S-1 h and S-100 h XRD profiles are remarkable, indicating that 1 h of vibrational milling is sufficient to nucleate stable SnSeS crystals. The microstructural stability of the SnSeS nanocrystals after 100 h of high-energy milling indicates a dynamical equilibrium where the exfoliation/restoration rate due to van der Waals forces is constant. The small peaks (indicated by arrows) in the S-1 h XRD pattern correspond to SnO_2 (ICSD card no. 39177).[23] No peaks of the precursor were observed after 1 h of milling. Pure Sn is relatively resistant to oxidation in ambient conditions. However, with the availability of oxygen atoms, the chemical environment provided by the Se atoms induces a strong tendency for the formation of SnO_2.[24] Figures 1(b)–1(d) show the Rietveld refinements of XRD patterns of the S-1 h, S-10 h, and S-100 h samples, respectively. Deconvolution of the XRD patterns illustrates a 10% increase of SnO_2 as we go from S-1 h to S-10 h. This is a collateral effect of the handling process as the S-1 h sample gets in touch with atmospheric oxygen when it is taken out from the milling vial to undergo XRD measurements. Since the Sn atoms become unstable in the presence of Se and O atoms, a careful control of the laboratory atmosphere is mandatory to follow the kinetics of Sn–Se alloy formation in *ex situ* investigations.

Figure 1(e) shows the DSC thermograms for the S-1 h and S-100 h samples. The S-1 h sample exhibits three exothermic peaks located at 101.5, 110.7, and 118 °C, as highlighted in the inset, which are absent in the thermograms of S-100 h sample. These peaks are attributed to the crystallization of amorphous selenium.[25] The amorphous Se presents different microstructures and transits to the trigonal structure releasing different amounts of energy at different temperatures.[26,27] The broad and exothermic band that follows from 120 °C to approximately 300 °C may be associated with the phase growth, increase of crystallite size, and reduction of defects and microstructural strains. The subtle endothermic peaks located at 114, 127, and 170 °C are attributed to structural phase transitions in sulfur.[28] Subsequently, the strong exothermic inclination, from 450 °C to 550 °C is attributed to the degradation of the samples promoting nucleation of SnO_2 crystals. The XRD measurements (not shown here) of the samples after the DSC measurements confirm this interpretation. In contrast, the S-100 h sample presents only a continuous release of energy with different slopes, which are attributed to defect reduction, crystallite growth, and SnO_2 formation. As we can see in Fig. 1(d), the XRD pattern of the S-100 h sample is relatively well simulated using just one SnSeS phase. Structural parameters and R-factors obtained from the Rietveld method are summarized in Table I.

Figure 2 shows the XRD pattern of sample S-100 h superimposed to the theoretical pattern calculated by using the Mercury program[29] with the crystallographic data obtained from the Rietveld refinement. It should be noted that the calculated pattern corresponds to a homogeneous and isotropic single polycrystalline phase, free of defects, size effects, or any other texture effect. One can clearly see that the experimental width and intensities of the XRD peaks are $h \, k \, l$-dependent. Disagreement in the relative intensities between the experimental and theoretical diffraction patterns in the {0 0 l} and {h 0 0} family peaks indicate a highly orientated sample. This discrepancy stems from the SnSeS layers and is adjusted by the Rietveld method, using the ODF model, reaching the texture index of 15.7. It is also observed that the experimental
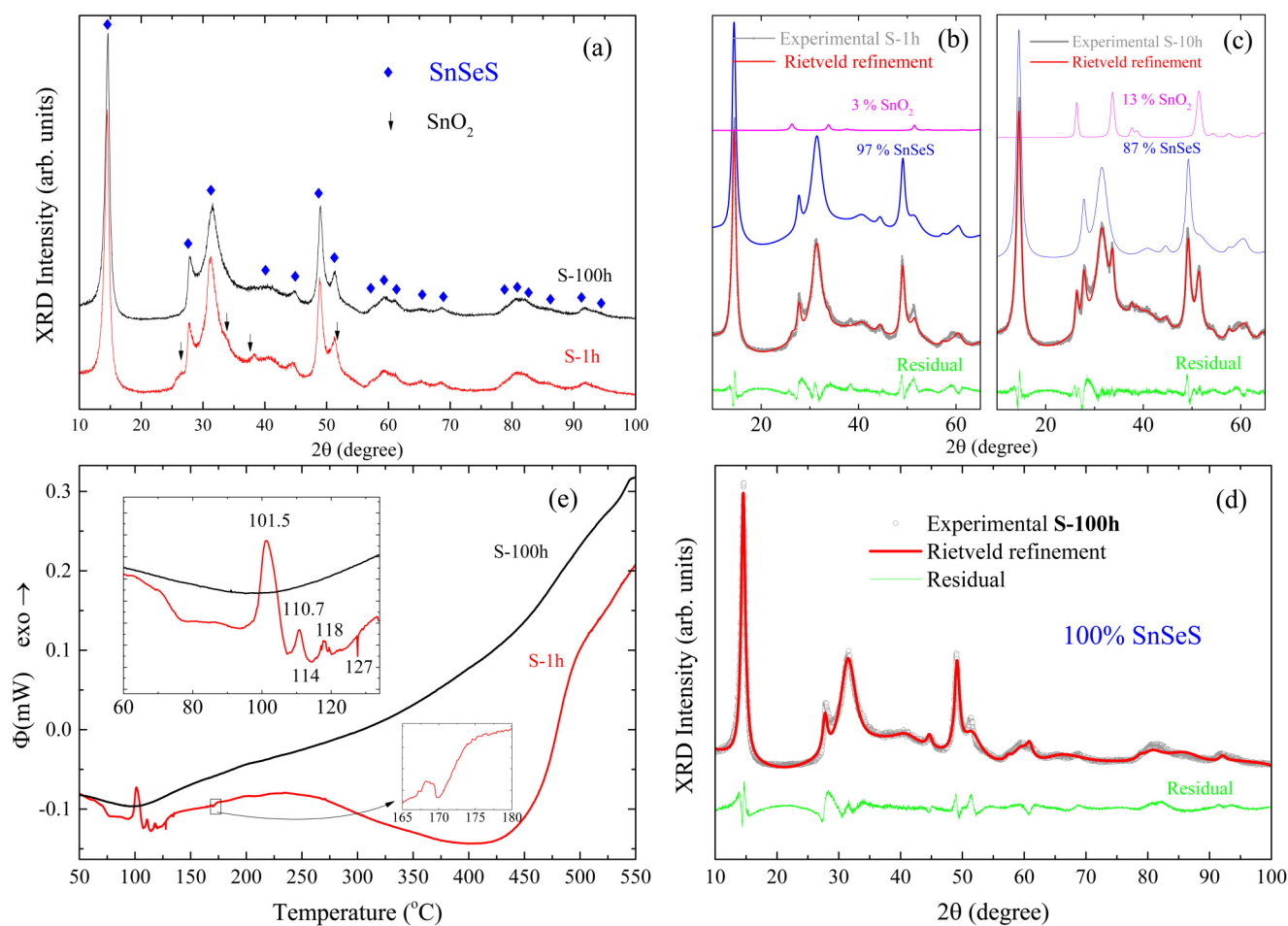
FIG. 1. (a) XRD patterns of the milled S-1 h and S-100 h samples. The arrows indicate the presence of impurities that arise from SnO_2 phase. Figures (b), (c), and (d) show the experimental XRD pattern of the S-1 h, S-10 h, and S-100 h samples superimposed with its respective best fitting achieved by the Rietveld method and its discriminated phase contributions. (e) DSC curves of the milled samples. The inset graphs highlight the details of the S-1 h sample.

peaks corresponding to the planes $(1\,0\,2)$ and $(1\,0\,{-}2)$, around $2\theta = 40°$, present atypical widening and reduction in their intensities and shape (peak-shape), which cannot be explained by the preferential orientation effect. It is known that the C6 structure, due to the presence of weak van der Waals forces between the layers, allows the formation of many different polytypes. The hexagonal

TABLE I. Lattice parameters for nanostructured $Sn_{34}S_{33}Se_{33}$ using space group $P\bar{3}m1$, obtained from the Rietveld method.

Sample	Lattice parameters (nm)	V (nm³)	R_{wp} (%)	χ^2
S-1 h	$a = 0.371\,24\,(4)$ $c = 0.612\,0\,(1)$	7.305 (2)	8.5	6.7
S-100 h	$a = 0.370\,77\,(5)$ $c = 0.609\,1\,(1)$	7.252 (2)	11.2	10.8

(2H) or rhombohedral (3R) structures are the most common ones.[30] As can be seen from Figs. 1(d) and 2, the main details of the XRD pattern were described by the trigonal/rhombohedral system, space group $P\bar{3}m1$, excluding the possibility of polytypism occurrence. The strong reduction in intensities is attributed, therefore, to structural defects of stacking faults and texture.[31,32] The anisotropic widening is well fitted utilizing the Stephens model. In order to estimate the apparent size of crystallites and microstrains, we have used Eqs. (5) and (6) for the four well-fitted peaks obtained by the Rietveld method, as shown in Table II. As expected, the microstructural parameters in these two samples are quite similar with average apparent crystallite sizes of ca. 6 nm and a high percentage of deformation, especially in the $(1\,0\,1)$ and $(1\,0\,2)$ planes.

Figures 3–5 show the HRTEM images of the S-100 h sample. Figure 3(a) corresponds to a randomly chosen particle representative of the powder. The corresponding electron diffraction pattern is shown in Fig. 3(b), indicating that the observed particle is
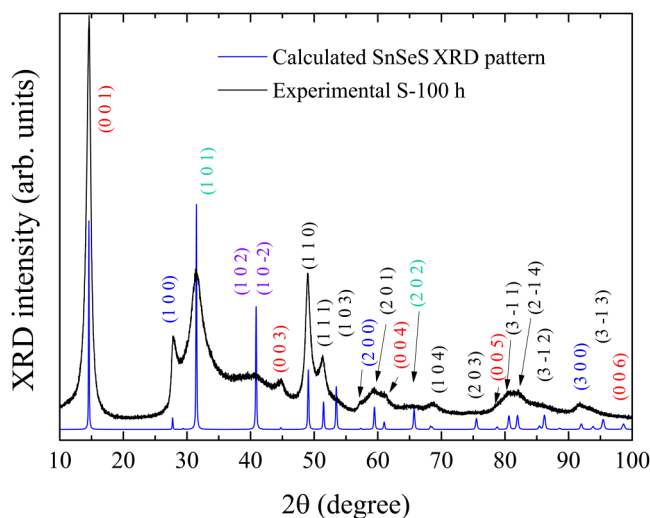
FIG. 2. XRD pattern of the S-100 h sample and the corresponding Rietveld refinement (blue curve).

polycrystalline in accordance with the XRD pattern taken for the entire sample with countless particles. In the region highlighted by the circle [Fig. 3(c)], we observe a "compacted" scenario—the layers are narrower and closer to each other (stacked planes). It is possible to note the continuity of the layers at the interface between defects and the crystal, indicated by the arrows in Fig. 3(d). This can be associated to the stacking fault defects observed in the XRD measurements. In Fig. 3(d), we see that this region of defects extends over a considerable region of the image, surrounded by crystallites oriented in different directions. In the inset, we show the Fourier transform of this region of defects, revealing the lines inclined to the (1 0 2) plane. This observation is totally consistent with the loss of intensity of the (1 0 2) and (1 0 −2) peaks as observed by the X-ray diffraction measurements. In Fig. 3(e), with an amplification, we see some cracks with small depth, without loss in the continuity of the layers, before and after the crack indicating a superficial defect.

Figure 4 shows a region away from the edges of the particle. Firstly, what draws our attention is the narrow region of the

TABLE II. Mean crystallites size and microstrains for samples milled by 1 h and 100 h.

Sample	$(h\,k\,l)$	D (nm)	$\langle D \rangle$ (nm)	ε (%)	ε (%)
S-1 h	(1 0 1)	3 (2)	6 (2)	2.2 (4)	1.8 (8)
	(1 1 0)	8 (1)		0.6 (5)	
	(0 0 1)	8 (1)		1.9 (3)	
	(1 0 2)	4 (7)		2.4 (4)	
S-100 h	(1 0 1)	3 (3)	6 (4)	2.5 (7)	1.9 (1)
	(1 1 0)	8 (1)		0.5 (7)	
	(0 0 1)	9 (2)		1.6 (5)	
	(1 0 2)	2 (3)		2.8 (5)	

interface between crystallites, that is, one crystallite begins practically where the other ends. We also see that the directions or angles of intercession between one crystallite and another have no preference and may even be orthogonal to each other. In the figure, we highlight a crystallite of 15 layers with compatible dimensions (D) as estimated by the analysis of line width shown in Table II. The regularity of the layers allows us to estimate their dimensions and we can compare them with those obtained by the analysis of XRD patterns. In the inset of Fig. 4, we highlight the delimited region and estimate the distances between the centers of the light fringes and the thickness of the dark fringes. The values obtained agree excellently with those obtained by XRD, as shown by the refined unit cell aside.

Figure 5 shows the HRTEM measurement oriented along the direction [0 0 1] of the crystal as shown by the Fourier transform (inset). In this projection, we observe aligned hexagons as illustrated by the adjacent unit cell, both in the dark field and in the light field. We can see several discontinuities and disordered distributions between light and dark fields. This is a characteristic that indicates the formation of stacks of layers and steps.[33]

Raman spectra have been used to examine the defect-dependent vibrational modes of the S-100 h sample, showed in Fig. 6. The Rayleigh wing[34] baseline was estimated by using a spline polynomial function with four points (orange solid curve and Raman peaks are fitted by using five Lorentzian functions).

Group theoretical symmetry analysis of the $Sn_{34}S_{33}Se_{33}$, CdI_2-type (space group $P\bar{3}m1$ and D_{3d} (−3 m) point group) yields four groups of phonons at Brillouin zone center, classified as infrared (IR), Raman and hyper-Raman active modes.[35]

$$\Gamma = \Gamma_{Raman} + \Gamma_{IR} + \Gamma_{acoustic} + \Gamma_{hyper\text{-}Raman},$$

where $\Gamma_{Raman} = A_{1g} + E_g$, $\Gamma_{IR} = A_{2u} + E_u$, $\Gamma_{acoustic} = A_{2u} + E_u$, and $\Gamma_{hyper\text{-}Raman} = A_{2u} + E_u$.[35] Generally the hyper-Raman mode is extremely weak and rarely observed in experiments.[36] In IR modes, the Se and S atoms vibrate in phase, opposite to Sn atom, while in the Raman modes, the chalcogenides atoms vibrate opposite to each other with the Sn atoms remaining stationary, as inversion center.[37] The expected wave numbers for the Sn–S and Sn–Se bonds are E_g (Sn–S) ~ 200 cm^{-1},[38] A_{1g} (Sn–S) ~ 315 cm^{-1},[38] E_g (Sn–Se) ~ 100 cm^{-1}, and A_{1g} (Sn–Se) ~ 185 cm^{-1}.[37] The observed peaks at 193 cm^{-1} and 294 cm^{-1} are attributed, therefore, to the vibrational modes E_g (Sn–S) and A_g (Sn–S), respectively. The shifts to low wavenumber may be attributed to the existence of Se atoms in the lattice that acts as vibrational inertia in the Sn–S active modes.

The wide peaks between 525 and 637 cm^{-1} are attributed to second-order effects, also in accord with SnS_2 reported in Ref. 39. The vibrational mode around 251 cm^{-1} in the nanostructured solid solutions $SnS_{2-x}Se_x$ may have two physical origins: either a symmetry breaking (loss of crystal periodicity), due to the presence of two interfaces (low dimensionality), as observed in other lamellar semiconductors with inversion center,[40] or a two-mode behavior of A_{1g} and E_g phonons, when the mass of one substituting element is smaller than the reduced mass of the compound formed by other two elements.[41,42] Since low-dimensional crystals were not observed in the HRTEM measurements, the explanation considering the two-mode Raman model is the most appropriate one.
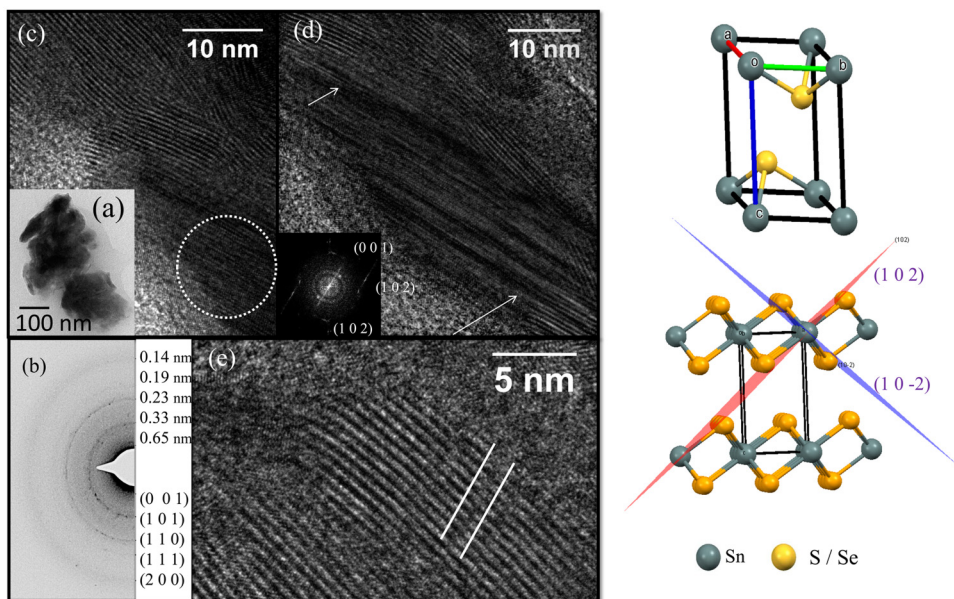
FIG. 3. HRTEM images of S-100 h sample. (a) Low magnification of particle under study. (b) Electron diffraction pattern. (c)–(e) Evidence of crystalline domains. The illustrated unit cell was obtained by using Rietveld refined results.

In a theoretical work, Gupta et al.[43] predict a Raman mode at around to $250 \, cm^{-1}$ by considering a mixed-layer SnS_xSe_{2-x} system. Their model considers that the sulfur and selenium atoms in the crystal distribute themselves randomly in the anion lattice sites in such a way that half of the sulfur atoms $(x/2)$ are in the upper layer and half are in the lower layer. Similarly, half of the selenium atoms $[(2-x)/2]$ are in the upper layer and half are in the lower layer. As we can see, the two-mode Raman model presumes some organizations, unexpected for samples made by high-energy milling. Thus, we believe that the observed $251 \, cm^{-1}$ Raman peaks are related to the Sn–Se bonds randomly distributed over the crystal lattice.

Figure 7 shows the UV-Vis absorbance spectrum of S-100 h sample recorded in the wavelength region of 180–1100 nm superimposed on their respective transformation obtained by using Eq. (8), assuming n = 2 (direct gap). We can observe from the experimental curve (blue line) that absorbance increases with decreasing wavelength, with the appearance of a shoulder at 275 nm. The absorbance analysis reveals a five-band structure with gaps located at 1.99, 2.60, 3.09, 3.66, and 4.56 eV.
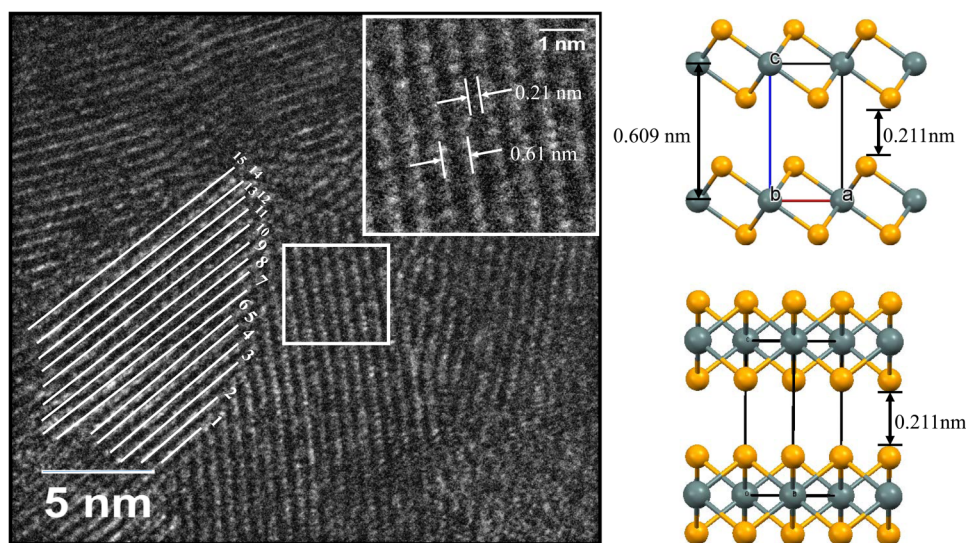

FIG. 4. HRTEM image of the S-100 h sample and unit cell obtained from Rietveld refinement results.
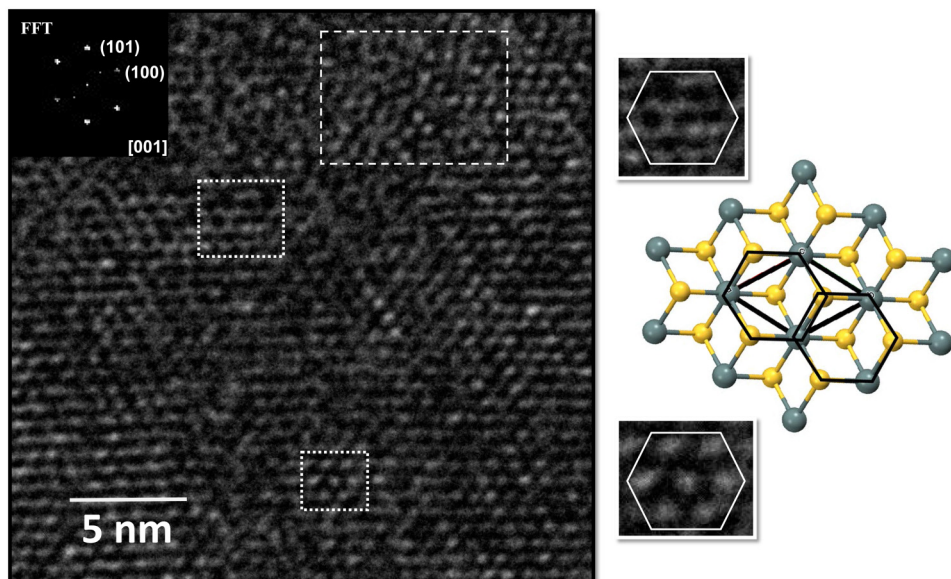
FIG. 5. HRTEM image of the S-100 h sample and unit cell in *c*-axis projection, obtained from Rietveld refinement results.

The origin of the multiple gap might be related either to the presence of any stoichiometric inhomogeneities present in the sample depending on the relative proportions of Se and S or to the inherent microstructural intricacies of the material. The first assumption is satisfied if the $SnS_{2-x}Se_x$ solid solutions exhibit a compositional dependence of the optical properties as reported in Ref. 7, where a tunable bandgap as a function of x has been observed. On the other hand, a very recent work shows clearly that the values of gap in layered-MoS_2[44] depend on the number of layers. In the present case of SnSSe ($SnS_{2-x}Se_x$ with x = 1), our XRD and Raman results indicate a very homogeneous sample, while HRTEM measurements, shown in Figs. 3 and 4, reveal different regions of crystallites with different sizes and layers. Thus, we assume that the appearance of multiple gap is related to the multilayer microstructure in the $SnS_{2-x}Se_x$, and not on the relative proportion of Se and S. Multiple gaps have also been found in similar orthorhombic crystalline structures with different morphologies (x = 0, for example) such as SnS_2 nanowires[45] nanocrystallites,[39] and flakes,[46] which strengthen our interpretation.
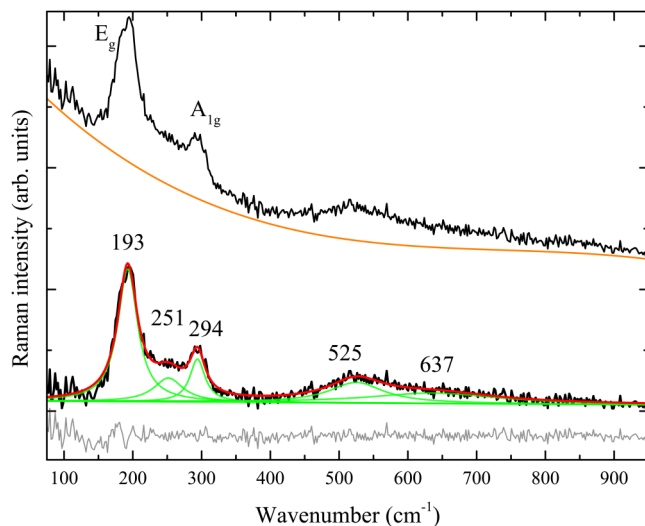
FIG. 6. Raman spectrum of the S-100 h sample. The upper curve shows the experimental curve and the background. The lower curve shows the Lorentzian fit from 5 vibrational modes after the background removal.
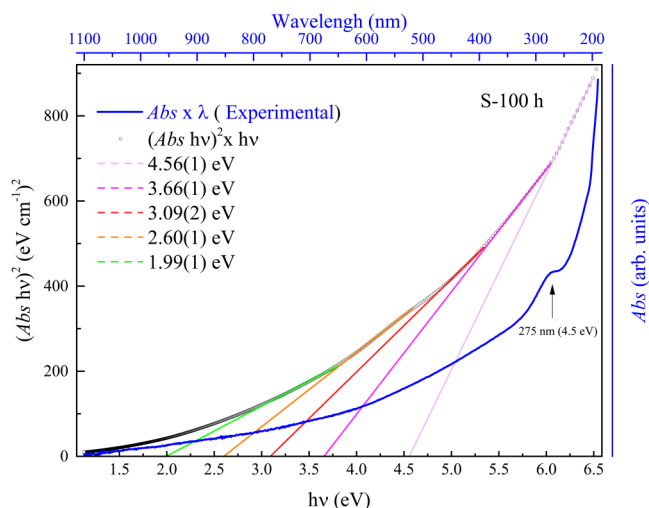
FIG. 7. UV-Vis absorbance spectrum of the S-100 h sample and the corresponding Tauc plot [Eq. (8)] for the bandgap calculation.

IV. CONCLUSIONS

In this work, we performed an investigation on the structural and optical properties of a single phase SnSSe solid solution obtained by high-energy milling. The lamellar nanocrystalline phase nucleates easily and can be obtained after 1 h of milling. The obtained SnSSe microstructure remains stable even after 100 h of milling.

By combining XRD, HRTEM measurements, and the Rietveld method, a detailed perspective of the microstructure was obtained, revealing crystallites mean sizes at around 6 nm, lamellar fractures, atomic vacancies, and stack-fault defects.

The observation of the two-mode Raman active lattice vibration confirms that the S/Se atoms are distributed randomly in the lattice.

The absorption spectrum of SnSSe solid solution contains five spectral intervals with characteristic shapes of direct allowed interband transitions with the effective bandgaps appearing around 623, 477, 401, 339, and 272 cm^{-1}. The origin of these multiple bandgaps might be associated with the multilayered microstructure present in $SnS_{2-x}Se_x$.

REFERENCES

[1]Y. Wu, W. Li, A. Faghaninia, Z. Chen, J. Li, X. Zhang, B. Gao, S. Lin, B. Zhou, A. Jain, and Y. Pei, Mater. Today Phys. **3**, 127 (2017).

[2]L.-D. Zhao, S.-H. Lo, Y. Zhang, H. Sun, G. Tan, C. Uher, C. Wolverton, V. P. Dravid, and M. G. Kanatzidis, Nature **508**, 373 (2014).

[3]W. J. Baumgardner, J. J. Choi, Y.-F. Lim, and T. Hanrath, J. Am. Chem. Soc. **132**, 9519 (2010).

[4]Y. Huang, E. Sutter, J. T. Sadowski, M. Cotlet, O. L. A. Monti, D. A. Racke, M. R. Neupane, D. Wickramaratne, R. K. Lake, B. A. Parkinson, and P. Sutter, ACS Nano **8**, 10743 (2014).

[5]Y.-M. Han, J. Zhao, M. Zhou, X.-X. Jiang, H.-Q. Leng, and L.-F. Li, J. Mater. Chem. A **3**, 4555 (2015).

[6]Asfandiyar, T.-R. Wei, Z. Li, F.-H. Sun, Y. Pan, C.-F. Wu, M. U. Farooq, H. Tang, F. Li, B. Li, and J.-F. Li, Sci. Rep. **7**, 43262 (2017).

[7]J. Yu, C. Y. Xu, Y. Li, F. Zhou, X. S. Chen, P. A. Hu, and L. Zhen, Sci. Rep. **5**, 17109 (2015).

[8]B. Pałosz, W. Pałosz, and S. Gierlotka, Acta Crystallogr. Sect. C **41**, 807 (1985).

[9]Z. Yang, H. Liang, X. Wang, X. Ma, T. Zhang, Y. Yang, L. Xie, D. Chen, Y. Long, J. Chen, Y. Chang, C. Yan, X. Zhang, X. Zhang, B. Ge, Z. Ren, M. Xue, and G. Chen, ACS Nano **10**, 755 (2016).

[10]Q. H. F. Rebelo, E. A. Cotta, S. M. de Souza, D. M. Trichês, K. D. Machado, J. C. de Lima, T. A. Grandi, C. M. Poffo, and L. Manzato, J. Alloys Compd. **575**, 80 (2013).

[11]E. Botcharova, M. Heilmaier, J. Freudenberger, G. Drew, D. Kudashow, U. Martin, and L. Schultz, J. Alloys Compd. **351**, 119 (2003).

[12]R. Young, *The Rietveld Method* (International Union of Crystallography, Oxford Science Publications, 1993), Vol. 312, ISBN: 0-19-855577-6.

[13]A. C. Larson and R. B. Von Dreele, Los Alamos National Laboratory Report LAUR 86-748 (2004).

[14]L. B. Mccusker, R. B. Von Dreele, D. E. Cox, D. Louer, and P. Scardi, J. Appl. Cryst. **32**, 36 (1999).

[15]A. Leineweber, Z. Kristallogr. **226**, 905–923 (2011).

[16]P. W. Stephens, J. Appl. Crystallogr. **32**, 281 (1999).

[17]V. K. Pecharsky and P. Zavalij, *Fundamentals of Powder Diffraction and Structural Characterization of Materials*, 2nd ed. (Springer, 2010), ISBN: 978-0-387-09579-0.

[18]C. A. Schneider, W. S. Rasband, and K. W. Eliceiri, Nat. Methods **9**, 671 (2012).

[19]A. V. J. Tauc, R. Grigorovici, and A. Vancu, Phys. Status Solidi B **15**, 627 (1966).

[20]B. D. Viezbicke, S. Patel, B. E. Davis, and D. P. Birnie, Phys. Status Solidi B **252**, 1700 (2015).

[21]N. Ghobadi, Int. Nano Lett. **3**, 2 (2013).

[22]J. Baltazar-Rodrigues, J. C. De Lima, C. E. M. Campos, and T. A. Grandi, J. Phys. Condens. Matter **20** 465205 (2008).

[23]A. Belsky, M. Hellenbrandt, V. L. Karen, and P. Luksch, Acta Crystallogr. Sect. B Struct. Sci. **58**, 364 (2002).

[24]S. Duhalde, B. Arcondo, E. Nassif, and H. Sirkin, Hyperfine Interact. **39**, 165 (1988).

[25]J. C. de Lima, T. A. Grandi, and R. S. De Biasi, J. Non-Cryst. Solids **286**, 93 (2001).

[26]G. J. Fan, F. Q. Guo, Z. Q. Hu, M. X. Quan, and K. Lu, Phys. Rev. B **55**, 11010 (1997).

[27]F. Q. Guo and K. Lu, Phys. Rev. B **57**, 10414 (1998).

[28]C. M. Kok, Eur. Polym. J. **21**, 579 (1985).

[29]C. F. Macrae, I. J. Bruno, J. A. Chisholm, P. R. Edgington, P. McCabe, E. Pidcock, L. Rodriguez-Monge, R. Taylor, J. Van De Streek, and P. A. Wood, J. Appl. Crystallogr. **41**, 466 (2008).

[30]Q. H. Wang, K. Kalantar-Zadeh, A. Kis, J. N. Coleman, and M. S. Strano, Nat. Nanotechnol. **7**, 699 (2012).

[31]G. A. Da Silva, D. M. Trichês, E. A. Sanches, K. D. Machado, C. M. Poffo, J. C. De Lima, and S. M. De Souza, J. Mol. Struct. **1074**, 511 (2014).

[32]M. Casas-Cabanas, M. R. Palacín, and J. Rodríguez-Carvajal, Powder Diffr. **20**, 334 (2005).

[33]E. G. Da Silveira Firmiano, A. C. Rabelo, C. J. Dalmaschio, A. N. Pinheiro, E. C. Pereira, W. H. Schreiner, and E. R. Leite, Adv. Energy Mater. **4**, 1301380 (2014).

[34]G. Gouadec and P. Colomban, Prog. Cryst. Growth Charact. Mater. **53**, 1 (2007).

[35]E. Kroumova, M. I. Aroyo, J. M. Perez-Mato, A. Kirov, C. Capillas, S. Ivantchev, and H. Wondratschek, Phase Transit. **76**, 155 (2003).

[36]V. N. Denisov, B. N. Mavrin, and V. B. Podobedov, Phys. Rep. **151**, 1 (1987).

[37]Chanchal and A. K. Garg, Physica B **383**, 188 (2006).

[38]J. M. Gonzalez and I. I. Oleynik, Phys. Rev. B **94**, 125443 (2016).

[39]C. Wang, K. Tang, Q. Yang, and Y. Qian, Chem. Phys. Lett. **357**, 371 (2002).

[40]S. M. Souza, D. M. Trichês, C. M. Poffo, J. C. de Lima, T. A. Grandi, and R. S. de Biasi, J. Appl. Phys. **109**, 013512 (2011).

[41]I. F. Chang and S. S. Mitra, Adv. Phys. **20**, 359 (1971).

[42]D. Walsh, S. Jandl, and J. Y. Harbec, J. Phys. C **13**, L125 (1980).

[43]H. C. Gupta, G. Sood, M. M. Sinha, and B. B. Tripathi, Phys. Rev. B **37**, 8370 (1988).

[44]B. Bergk, U. Mühle, I. Povstugar, N. Koutná, D. Holec, H. Clemens, and B. Kieback, Acta Mater. **144**, 700 (2018).

[45]Y.-T. Lin, J.-B. Bin Shi, Y.-C. Chen, C.-J. Chen, and P.-F. Wu, Nanoscale Res. Lett. **4**, 694 (2009).

[46]C. Fan, Y. Li, F. Lu, H.-X. Deng, Z. Wei, and J. Li, RSC Adv. **6**, 422 (2016).